High-Resolution Multi-Scale Computational Model for Non-Invasive Cervical Vagus Nerve Stimulation

Article *in* Neuromodulation · October 2017

DOI: 10.1111/ner.12706

CITATIONS
7

READS
182

5 authors, including:

Antonios Mourdoukoutas
University of California, Berkeley
5 PUBLICATIONS **251** CITATIONS

SEE PROFILE

Dennis Truong
City College of New York
72 PUBLICATIONS **1,059** CITATIONS

SEE PROFILE

Marom Bikson
City College of New York
414 PUBLICATIONS **11,883** CITATIONS

SEE PROFILE

Received: May 12, 2017 Revised: July 26, 2017 Accepted: August 25, 2017

(onlinelibrary.wiley.com) DOI: 10.1111/ner.12706

High-Resolution Multi-Scale Computational Model for Non-Invasive Cervical Vagus Nerve Stimulation

Antonios P. Mourdoukoutas, BE*; Dennis Q. Truong, MS*; Devin K. Adair, BA†; Bruce J. Simon, PhD‡; Marom Bikson, PhD*

Objectives: To develop the first high-resolution, multi-scale model of cervical non-invasive vagus nerve stimulation (nVNS) and to predict vagus fiber type activation, given clinically relevant rheobase thresholds.

Methods: An MRI-derived Finite Element Method (FEM) model was developed to accurately simulate key macroscopic (e.g., skin, soft tissue, muscle) and mesoscopic (cervical enlargement, vertebral arch and foramen, cerebral spinal fluid [CSF], nerve sheath) tissue components to predict extracellular potential, electric field (E-Field), and activating function along the vagus nerve. Microscopic scale biophysical models of axons were developed to compare axons of varying size (Aα-, Aβ- and Aδ-, B, and C-fibers). Rheobase threshold estimates were based on a step function waveform.

Results: Macro-scale accuracy was found to determine E-Field magnitudes around the vagus nerve, while meso-scale precision determined E-field changes (activating function). Mesoscopic anatomical details that capture vagus nerve passage through a changing tissue environment (e.g., bone to soft tissue) profoundly enhanced predicted axon sensitivity while encapsulation in homogenous tissue (e.g., nerve sheath) dulled axon sensitivity to nVNS.

Conclusions: These findings indicate that realistic and precise modeling at both macroscopic and mesoscopic scales are needed for quantitative predictions of vagus nerve activation. Based on this approach, we predict conventional cervical nVNS protocols can activate A- and B- but not C-fibers. Our state-of-the-art implementation across scales is equally valuable for models of spinal cord stimulation, cortex/deep brain stimulation, and other peripheral/cranial nerve models.

Keywords: Cranial nerve stimulation, electrode placement, mechanisms of action, neurostimulation, stimulation, vagus nerve stimulation

Conflict of Interest: Dr. Simon is an employee of electroCore and has shares in the company. The City University of New York has patents on brain stimulation with Dr. Bikson as inventor. Dr. Bikson also has equity in Soterix Medical Inc. and serves as a scientific advisor to Boston Scientific Inc. The remaining authors have no relevant conflicts to disclose.

BACKGROUND

Neuromodulation using vagus nerve stimulation (VNS) is a promising treatment for a range of central and peripheral disorders. The vagus nerve is the primary parasympathetic branch of the autonomic nervous system regulating multiple organ systems including breathing, heart rate, peristalsis, and gastric emptying. It also plays an important role in the regulation of the body's inflammatory responses, through an anti-inflammatory pathway mediated by acetylcholine (1,2). VNS is a potential strategy for treating inflammatory conditions like rheumatoid arthritis and Crohn's disease (1–3), increasing brain training and rehabilitation (4–7), and direct or adjunctive therapy for the treatment of epilepsy (8,9), depression (10,11), stroke (12–14), tinnitus (15,16), headache (17,18), traumatic brain injury (19–21), posttraumatic stress disorder (PTSD) (22,23), and Alzheimer's disease (24,25).

Invasive VNS, with an implanted pulse generator and electrodes coiled around the cervical branch of the vagus, is FDA approved for the treatment of medically refractory epilepsy and major depressive disorder (MDD) (26,27). For the treatment of epilepsy, VNS has been shown to reduce both seizure frequency and severity (8,9). In patients with MDD symptom severity is reduced, (10,11), though long-term follow-up is still ongoing (28).

Non-invasive stimulation of the vagus nerve has been developed, using transcutaneous stimulation to target the auricular branch of the vagus nerve at the concha of the outer ear (5,11,16,29,30) or the cervical branch of the vagus at the neck (13,18,31,32). These devices

Address correspondence to: Dennis Q. Truong, MS, Center for Discovery and Innovation, 85 St. Nicholas Terrace, New York, NY 10031, USA. Email: dtruong@ccny.cuny.edu

* Department of Biomedical Engineering, The City College of New York, City University of New York, New York, NY, USA;
† Department of Psychology, The Graduate Center, City University of New York, New York, New York, USA; and
‡ electroCore LLC, Basking Ridge, NJ, USA

For more information on author guidelines, an explanation of our peer review process, and conflict of interest informed consent policies, please go to http://www.wiley.com/WileyCDA/Section/id-301854.html

Source(s) of financial support: Dr. Bikson is supported by NIH (grants 1R01NS101362-01, 1R01MH111896-01, 1R01NS095123-01, 1R01MH109289-01).

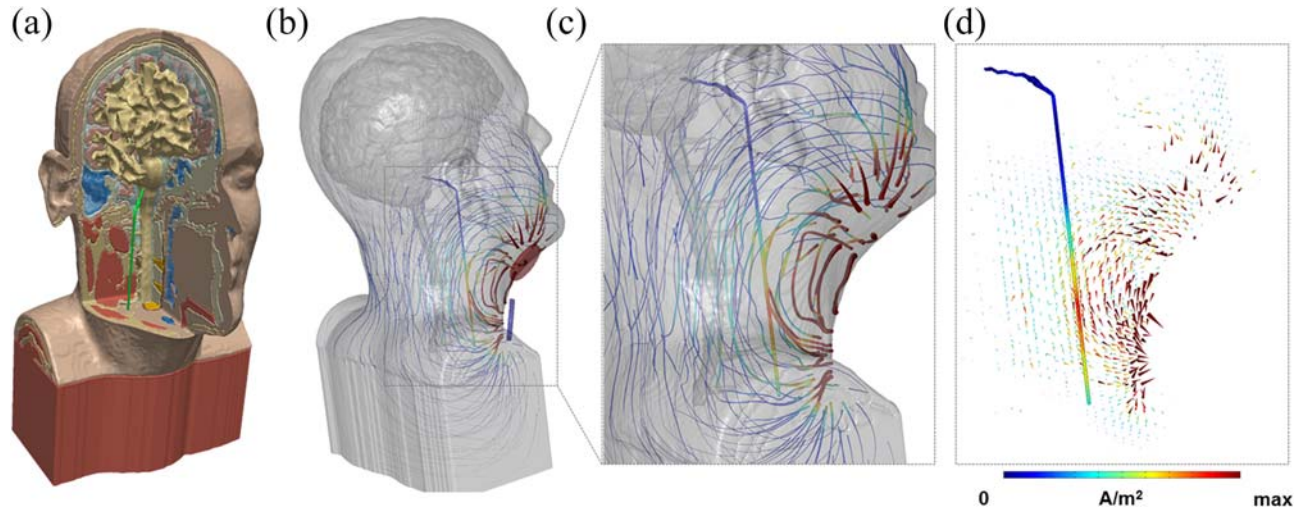

Figure 1. High-resolution model of nVNS current flow. a. MRI derived model including bone, brain, muscle and other soft tissue masks, and vagus nerve (green). b. Stimulation of nVNS with electrode placement showing flux lines map gross current flow patterns through neck, with false color of local current density (>10 A/m^2 max). Gross current flow patterns are determined by electrode position and anatomy. c. Inset showing expansion of current flow around vagus nerve (1.44 A/m^2 max) using the given electrode montage. d. Arrow plots of gross current density pattern and current density on vagus nerve in false colors. The current density (proportional to electric field) along the nerve supports the prediction of activation, depending on fiber type. All models are under the quasi-static assumption with the anode in red and cathode in blue for illustration of instant direction. [Color figure can be viewed at wileyonlinelibrary.com]

do not require surgical implantation of a stimulator (33) and therefore have the potential to dramatically increase accessibility to VNS. Cervical nVNS (gammaCore, electroCore LLC, Basking Ridge, NJ, USA) has now been FDA approved for the acute treatment of pain associated with episodic cluster headache (32).

Despite the significant advances in the science and technology of nVNS, questions remain about optimal treatment paradigms, including signal amplitude and dosing regimen. Computational current flow and neuron activation models underpin brain stimulation design. Prior modeling efforts have focused on invasive VNS or peripheral nerve stimulation in general, but have not included the macroscopic and mesoscopic details that may be relevant to nVNS (34–37). Invasive VNS protocols typically have electrode cuffs positioned directly on the nerve itself, whereas nVNS electrodes are in contact with skin. These prior studies examined the influence of intermediary tissue (scar tissue) relevant to invasive stimulation, but much more tissue exist between nVNS electrodes and the nerve. In this study, a multi-scale computational approach was taken to predict the cellular targets of cervical nVNS—an essential step toward elucidating and optimizing both treatment and mechanisms. Indeed, our results using an exemplary dose show the importance of previously unrecognized precision in modeling methods (including local tissue) in prediction fidelity.

METHODS

High resolution T1 and T2 MRI-scans (1 mm^3 voxels) extending between the C7 vertebra and the vertex were segmented into 11 tissue masks using automated algorithms and manual segmentation techniques as previously described (1). The MRI-derived model is the first to accurately reproduce details of macroscopic (e.g., skin, muscle) and mesoscopic (vertebra, cerebral spinal fluid [CSF], anatomical details, nerve sheath) tissues (Fig. 1). T1-weighted scans were collected using a GRE sequence with a TR of 1900 msec, TE of 2.2 msec. T2-weighted scans were collected using a SPACE sequence with a TR of 3200 msec and TE of 402 msec. Automated segmentation algorithms were used to create an initial six tissue (skin, skull, CSF, gray matter, white matter, air/sinus) model (38,39). Post processing filters were used to smooth, close holes and discontinuities, and remove floating voxel artifacts in skull, CSF, and gray matter (39). Additional tissues and anatomical detail was manually segmented in ScanIP (Simpleware, Synopsys, Exeter, UK) to include fat, muscle, intervertebral disk, and ligaments. Three levels of anatomical detail were prepared, which consisted of uniform soft tissue (skin, fat, ligament and intervertebral disk merged) and a single mask vagus nerve, full anatomical detail with the vagus nerve encapsulated in a connective tissue sheath, and full anatomical detail with a single mask vagus nerve (no tissue sheath) (Fig. 1).

An adaptive tetrahedral mesh was generated using voxel-based meshing algorithms contained in ScanIP (Simpleware, Synopsys). Multiple mesh densities were refined to within a 1% error in voltage and current density at the vagus nerve resulting in a model size of approximately 30M tetrahedral elements for the full anatomy model. Finite element method (FEM) models were generated using the aforementioned meshes in COMSOL Multiphysics to simulate current flow generated through the neck during stimulation. We modeled an nVNS bipolar electrode montage with two, 2 cm radius electrodes separated (center to center) by 4 cm, positioned over the cervical vagus nerve. The Laplace equation for electrostatics ($\nabla \cdot (\sigma \nabla V) = 0$) was applied and solved as the field equation given: insulated ($J \cdot n = 0$) external boundaries, a normal current density equivalent to 30 mA ($(J \cdot n)^* Area_{anode} = 30$ mA) on the anode, and a ground ($V = 0$) condition on the cathode. Results were linearly scaled to assess different stimulation intensities corresponding to typical currents used clinically.

The voltage profile along the vagus nerve solved for in FEM simulations was sampled into 1000 transverse slices at a Δx of 0.14 mm along the nerve. We considered three related "driving functions" for local nerve stimulation that are fiber independent, and a fourth biophysical fiber specific neuron model. The driving functions where 1) electric field (E-Field) magnitude (40–42), which is a reasonable predictor of polarization under the quasi-uniform assumption (43)—especially with complex neuronal morphology; 2) E-Field magnitude along the vagus nerve, which more directly approximates

polarization at terminals, branch, and membrane property changes (44–46); 3) derivative of E-Field along the nerve, which is called the "activating function" and determines local transmembrane current drive (47,48). All these driving functions have been previously considered (49,50) and it is beyond the scope of this paper to judge superiority, but each driving function is derived from the prior one, and contrasting them facilitates understand the role of tissue segmentation detail across this chain—which is an innovation of our work-flow.

For the neuron model, the average voltage of each slice was projected into micro-scale models in NEURON (51) to predict nerve activation. Previous studies analyzing compound action potentials in vagus nerves have categorized fibers into three groups: A- (Aα-, Aβ-, and Aδ-), B-, and C-fibers (52,53). Voltages were applied as extracellular potentials on a long axon (145 mm) with diameters corresponding to A, B, and C fibers (22, 10, 1 μm). Active and passive parameters were assigned using values from literature (54,55). We developed an approach whereby we modeled rheobase thresholds, namely the response to a long duration pulse. This allowed us, as a first approximation, to remove considerations of neuron dynamics and stimulation train parameters such a number, pulse shape, frequency, and duty-cycle which while important (56–59) would incur a large set of addition fiber specific parameterizations (34,60–64)—whereas our focus was to address the role of tissue modeling. The assumption also supports future efforts to optimize stimulation approaches leveraging linearity (see "Discussion" section). Indeed, the wave parameters of the only currently FDA approved nVNS device, gammaCore, are close to rheobase (65).

Cervical, vagus nerve depth from the gammaCore electrodes was measured by ultrasonography. The average distances from the electrode surfaces to the vagus nerves were 1.27 ± 0.20 and 1.24 ± 0.26 cm for the right and left sides, respectively, so an average of 1.25 cm was used for the modeling (66).

RESULTS

For non-invasive vagus nerve stimulation (nVNS), current applied through electrodes on the neck must penetrate $\sim$1.25 cm through varied soft tissue (e.g., muscle) from the skin surface. The overall current path may be influenced by details of head shape (e.g., neck circumference) and deeper tissues (e.g., vertebra). As a first step to model nVNS, we adapted and enhanced a high-resolution model of the head and neck, and simulated current flow using an exemplary macro-electrode montage (Fig. 1). Given the complexity of the anatomy (67), we considered several levels of detail and tissue properties to understand sensitivity to model parameters. The role of macro-scale detail was considered by comparing a realistic inhomogeneous model (with each tissue assigned a specific resistivity) with a homogenous model (where all tissues were assigned the same resistivity), and by altering—on both models—the resistivity of the bulk soft tissue (Fig. 2). The role of meso-scale detail was considered by adding an insulating tissue sheath around the vagus nerve (Fig. 2), as well as by evaluating the role of local tissue changes around the nerve (Fig. 3). Finally, micro-scale stimulation of specific nerve activation was modeled across these conditions supporting predictions of sensitivity and selectivity.

Stimulation with macro surface electrodes produced current flow throughout the neck that rapidly decreased with distance from the surface $>$1.5 cm (Fig. 1). At the depth of the vagus nerve ($\sim$1.2 cm) the local current density maximum was between the two electrodes. E-field can be quantified by considering intensity along the vagus nerve under various model assumptions (Fig. 2). In the homogenous model (Fig. 2a) the E-field magnitude (Fig. 2a, top) roughly reflected distance from the stimulation electrodes, and E-field directed along the nerve even more so (Fig. 2a, middle). The derivative of the E-field along the nerve (Fig. 2a, bottom) was then a bi-modal profile, with a peak limited by the gradual rate of spatial change of the E-field. Changing tissue resistivity produced an expected linear scaling of all these driving terms.

In contrast to the homogenous case, for the inhomogeneous models, both without (Fig. 2b) and with (Fig. 2c) a sheath, predicting driving functions were not smooth. While there was a general trend to decrease with distance from the electrode (at large distances from the electrodes there is no significant generated current flow), meso-scale tissue changes resulted in local maxima. The role of local tissue (resistivity) changes in this profile is supported by their co-localization with changes in tissue type (Fig. 3) and by the dulling of the fluctuations by the inclusion of a sheath (Fig. 2c), which essentially dampens the influence of other local tissues. For the most direct measure of polarization along long axons, using the activating function (Fig. 2b,c bottom row), the resulting maximum and minimum are also determined by this tissue inhomogeneity—namely when the nerve passes through tissues of varying resistivity there is an associated change in activating function. In the inhomogeneous models, increasing bulk tissue resistivity generally increases driving functions, but with region specific scaling factors, and the location of activating function peaks remains unchanged. To our knowledge this is the first demonstration that meso-scale tissue properties, namely the extension of the vagus nerve through high and low resistivity surrounding tissues, is the governing factor in determining driving functions in nVNS. Moreover, despite the presence of sheaths around major nerves, this is the first modeling of effects of current flow around a nerve. Overall, these results strongly support the importance of state-of-the-art detail in segmentation.

Finally, we considered resulting activation of axon sub-types in the vagus nerve, with separate analysis for the three scales of model detail. The ranking order of sensitivity of A-fibers, followed by B-fibers, and then C-fibers did not change across all modeled conditions (Table 1), consistent with long-standing theory on fiber size and recurrent order (62,68,69). However, the absolute thresholds (applied nVNS current) varied across models, as expected given changes in the activating function (Fig. 2c, bottom). At stimulation intensities comparable to clinical nVNS protocols, the current flow patterns and nerve neurophysiology resulted in preferential activation of A-fibers and large B- fibers. This is consistent with clinical and animal studies showing nVNS effects mediated by vagus firing of predominantly A- and large B- fibers but not the smaller, myelinated B or nonmyelinated C fibers responsible for producing bradycardia and bronchoconstriction (70,71).

DISCUSSION

We developed a state-of-the art computational model to support the interpretation and design of cervical nVNS protocols. We emphasize the difference between a model with "complexity" but without accuracy (i.e., detail for its own sake, incorrectly segmented tissue compartments) and accurate models that prioritize accurate segmentation of the most relevant tissues (67). The latter requires careful *a priori* knowledge about structure-function that may exceed resolution of the anatomical (MRI) scans but none-the-less profoundly influences current flow patterns, including tissue continuity.

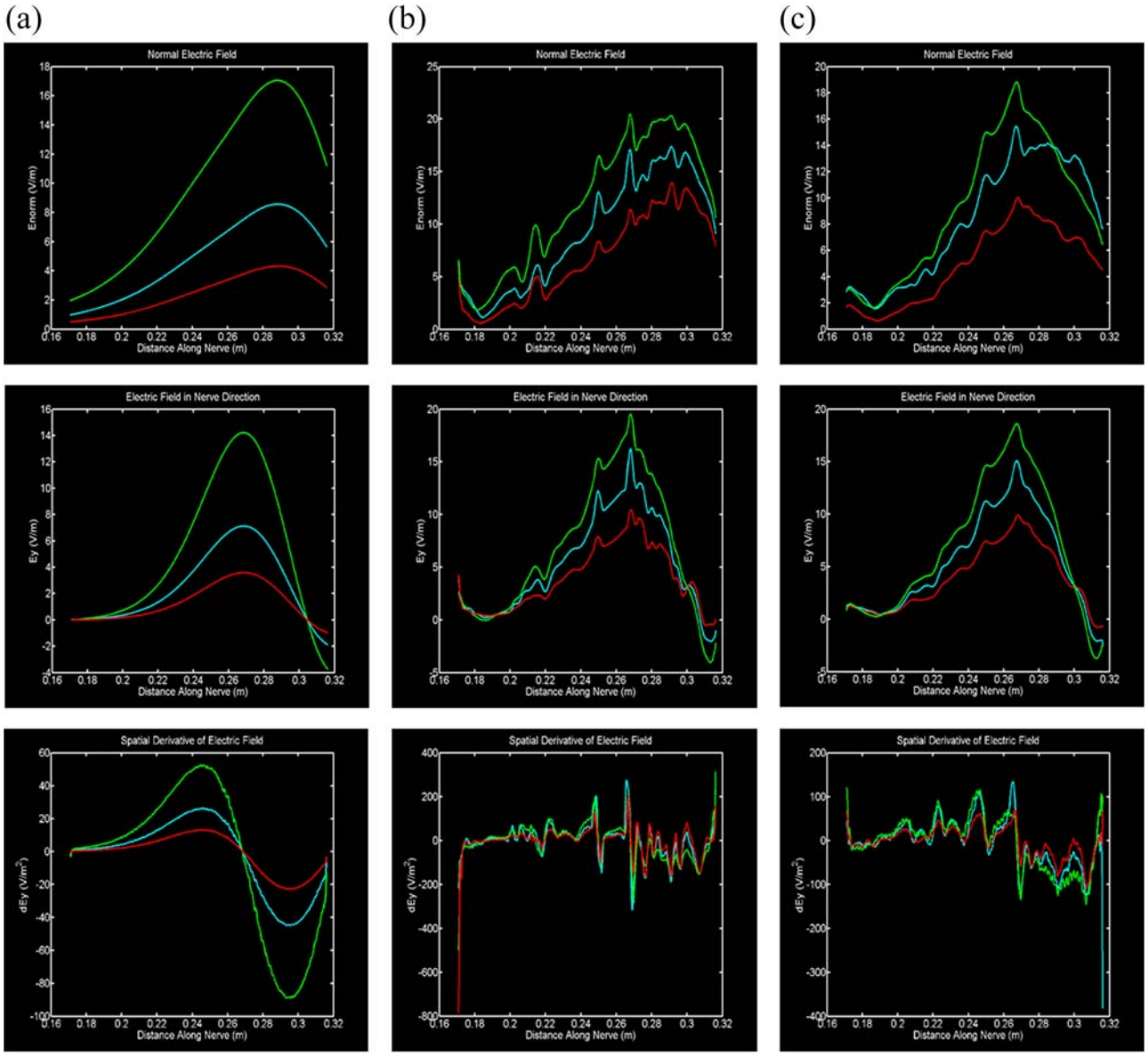

Figure 2. Role of tissue properties around nerve in predicting driving forces for activation. Three drivers of neuronal polarization: Electric field magnitude (top row), electric field component aligned with the nerve (middle row), and spatial derivative of electric field (activating function) in the direction of the nerve (bottom row). Three conditions of tissue detail are modeled. a. simplified homogenous soft tissue (muscle, fat, ligament, intervertebral disk merged) (first column); b. full inhomogeneous soft tissue anatomy without a fat sheath surrounding the vagus nerve (second column); c. full inhomogeneous soft tissue anatomy with a fat sheath surrounding the vagus nerve (third column). In each case, soft tissue conductivity was doubled (red), unaffected (blue), and halved (green). Whereas in a simplified homogeneous soft tissue case, a. drivers of activation are smooth, with full inhomogeneous soft tissue anatomy; b and c. local maximum are observed (0.217 m, 0.250 m, and 0.269 m) corresponding to changing tissue around the nerve (see Fig. 3). The addition of a sheath generally dulls the influence of these transitions. [Color figure can be viewed at wileyonlinelibrary.com]

Our model workflow advances nerve stimulation modeling at the macro- (cm) and meso- (mm) scales (Fig. 1). At the meso-scale, unlike geometric models generated using CAD (34,36,72), our model captures idiosyncratic differences in anatomy that influence current clustering (Fig. 2). At the same time, our findings emphasize that highly "detailed" models that do not validate segmentation accuracy (73,74) are subject to spurious results. Our simulations indicate that the inhomogeneous properties of tissue immediately surrounding nerves strongly influence membrane polarization by stimulation. Passage of axons along tissues with varied conductivities (e.g., soft tissue to bone) leads to a sudden change in E-Field (activating function) that, in turn, increases axon membrane polarization (Fig. 2b). However, the presence of encapsulating tissue, such as a fat sheath, can effectively dull these E-Field transients, reducing axon membrane polarization (Fig. 2c). In contrast to the role of local tissue properties, macro-scale tissue properties (tissue between the electrodes and the nerve) influence the total current delivered near the target, which scales the E-Field along the axon (Fig. 3, colored lines) ultimately influencing polarization magnitude.

Our approach to modeling nerve activation was heuristic but supported by more sophisticated biophysical studies. The maximal polarization achieved at any given intensity, for arbitrarily long pulses, was predicted by the response to a DC (static) field. Moreover, this step function-based threshold should approximate polarization achievable by optimized pulse trains—based on consideration of single cell dynamics as a low-pass filter. This step is methodologically

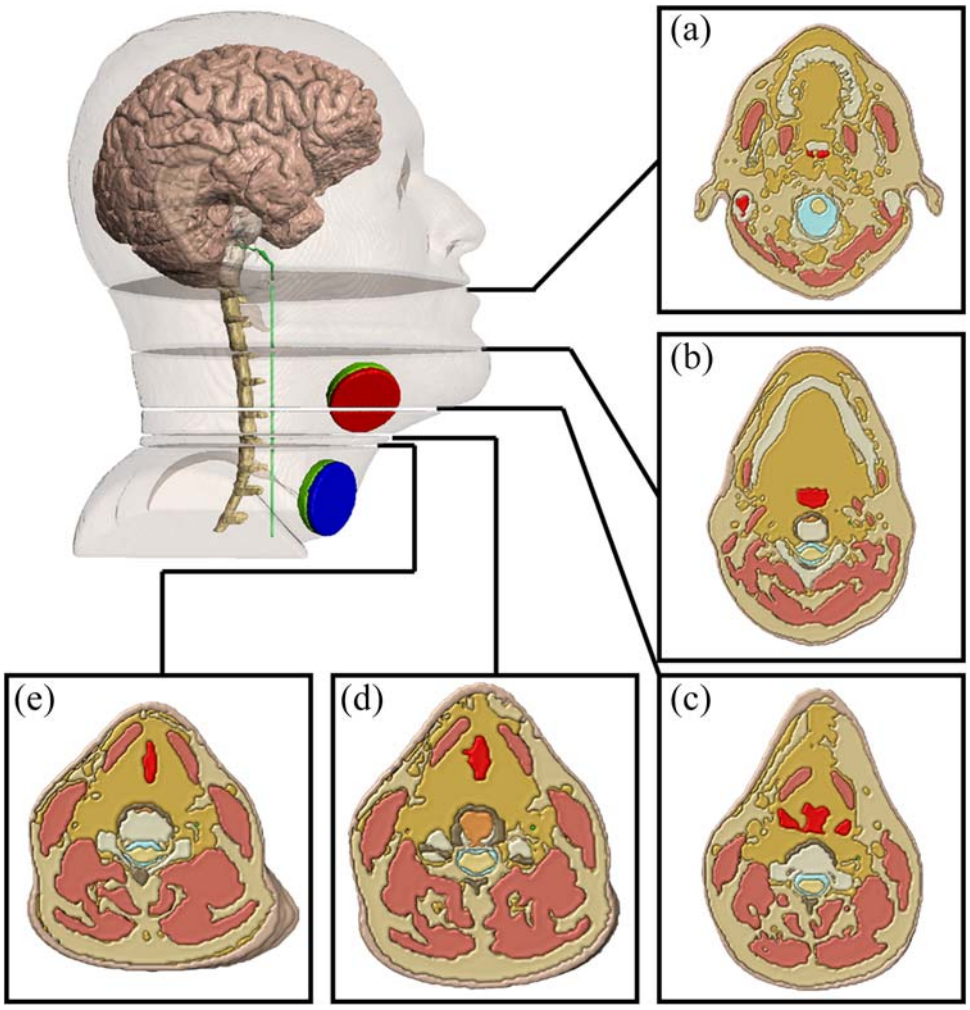

Figure 3. Illustration of local tissue in homogeneity around nerve leading to transients in drivers of activation. a. 0.180 m. b. 0.217 m. c. 0.250 m. d. 0.263 m. e. 0.269 m. Five anatomical cross sections showing cases in which either fat and soft tissue, a, b, c, e, or just fat, d, borders the vagus nerve. Slices-b, c, d, e are relatively close to the stimulating electrodes while slice-a is relatively far. [Color figure can be viewed at wileyonlinelibrary.com]

important and novel as it linearizes an otherwise complex optimization problem. This method ignores nonlinear contributions of complex membrane dynamics (e.g., resonance) (75) or synaptic (76) and network effects (77), but is especially reasonable for axons of passage (axons that do not terminate or initiate near the electrodes) (78) as the case for cervical VNS. Using step-function based thresholds would not capture relative differences in strength-duration (e.g., chronaxie) between fiber types such as A and C (79).

As linearity is preserved, this approach lends itself to efforts to automatically optimize stimulation approaches (67). For any given axon morphology and biophysics, electrode montage, and tissue properties, the stimulation current threshold to activate an action potential can be calculated. In turn, this means that (given the same

Table 1. Nerve Fiber Threshold and Activation Selectivity Under Varied Tissue Models.

	(A)				(B)				(C)		
Rheobase:	1 mA	10 mA	30 mA	Rheobase:	1 mA	10 mA	30 mA	Rheobase:	1 mA	10 mA	30 mA
A (22 μm)	×	✓	✓	A (22 μm)	✓	✓	✓	A (22 μm)	×	✓	✓
B (10 μm)	×	✓	✓	B (10 μm)	×	✓	✓	B (10 μm)	×	✓	✓
C (1 μm)	×	×	×	C (1 μm)	×	✓	✓	C (1 μm)	×	×	✓

For each stimulation current, a check indicates action potential generation (current above rheobase threshold) while a cross indicates no action potential generation (current below rheobase threshold). (A) Condition of full soft tissue compartment. (B) Condition of full anatomy without a fat sheath surrounding the vagus nerve. (C) Condition of full anatomy with a fat sheath surrounding the vagus nerve. In general, the lowest thresholds were predicted for the condition of full anatomy without sheath (B) corresponding to the most significant driving functions (Fig. 2). For a similar reason, addition of a sheath in the full model (C) slightly increases thresholds. In all cases, thresholds decreased for larger nerves. Macro- and meso-scale anatomical details thus influence predictions on fiber type activation threshold and so selectivity.

electrode montage and modeling assumptions) for any given applied current, which axons can be activated (assuming optimized waveform) can be predicted. This in turn allows understanding axon recruitment and selectivity for any given stimulation approach (independent of waveform), and supports tractable optimization efforts using a look-up-table matching stimulation dose with axon threshold. Importantly, accurate modeling of tissue properties (see above) can categorically influence activation prediction (Table 1). Our modeling advancements for macro/mesa-scale current flow (based on tissue representation) and micro-scale nerve activation (DC-Rheobase look-up-table) generalize to a wide range of brain stimulation models spanning spinal cord stimulation (72,73,80), cortex/deep brain stimulation (81–83), and peripheral/cranial nerve stimulation (48,84,85).

In trying to encompass the scale needed for non-invasive stimulation, some limitations did arise. Previous VNS models (34,36,37,86,87) have considered finer physiological detail including distribution of fibers in fascicles, varying fiber dynamics, blockage threshold, and the presence of local polarity peaks (virtual anode and cathodes). These studies can be leveraged in future work to develop more physiologically detailed models. Future models of nVNS can explore the effects of interindividual anatomical differences, varied electrode designs and locations (88), and experimental validation of current flow and target engagement (89–92).

Notwithstanding these potential refinements, the methods developed in this study provide a foundation for modeling nVNS from macroscale image-derived data, including the ability to predict nerve sensitivity and selectivity. This workflow is exemplified for the case of non-invasive electrical stimulation of the cervical vagus nerve. We predicted, using a specific electrode montage, that at a typical clinical applied current of $\sim$ 10 mA, E-Fields produced along the right vagus nerve are sufficient to activate A-fibers and larger B-fibers but not C-fibers (based simply on fiber diameter) These models support emerging clinical evidence of efficacy and tolerability (18,29,31,32) that properly designed nVNS is a targeted neuromodulation tool, and can be an alternative to an implanted stimulator, without the associated morbidities.

Authorship Statement

Dr. Bikson, Dr. Simon, and Mr. Mourdoukoutas designed the study. Mr. Mourdoukoutas built the model and ran the simulations. Mr. Mourdoukoutas, Mr. Truong, and Mr. Adair analyzed the data and prepared the figures. Dr. Bikson, Dr. Simon, and Mr. Mourdoukoutas drafted the text with important intellectual input from Mr. Truong and Mr. Adair. All authors approved the final manuscript.

How to Cite this Article:

Mourdoukoutas A.P., Truong D.Q., Adair D.K., Simon B.J., Bikson M. 2017. High-Resolution Multi-Scale Computational Model for Non-Invasive Cervical Vagus Nerve Stimulation.
Neuromodulation 2017; E-pub ahead of print. DOI:10.1111/ner.12706

REFERENCES

1. Tracey KJ. Physiology and immunology of the cholinergic antiinflammatory pathway. *J Clin Invest* 2007;117:289–296.
2. Bonaz B, Picq C, Sinniger V, Mayol J-F, Clarençon D. Vagus nerve stimulation: from epilepsy to the cholinergic anti-inflammatory pathway. *Neurogastroenterol Motil* 2013;25:208–221.
3. Zhou L, Lin J, Lin J, Kui G, Zhang J, Yu Y. Neuroprotective effects of vagus nerve stimulation on traumatic brain injury. *Neural Regen Res* 2014;9:1585.
4. Hays SA, Rennaker RL, Kilgard MP. Targeting plasticity with vagus nerve stimulation to treat neurological disease. *Prog Brain Res* 2013;207:275.
5. Van Leusden JW, Sellaro R, Colzato LS. Transcutaneous Vagal Nerve Stimulation (tVNS): a new neuromodulation tool in healthy humans? *Front Psychol* 2015;6:102.
6. Porter BA, Khodaparast N, Fayyaz T et al. Repeatedly pairing vagus nerve stimulation with a movement reorganizes primary motor cortex. *Cereb Cortex* 2012;22:2365–2374.
7. Hays SA. Enhancing rehabilitative therapies with vagus nerve stimulation. *Neurotherapeutics* 2016;13:382–394.
8. Panebianco M, Rigby A, Weston J, Marson AG. Vagus nerve stimulation for partial seizures. *Cochrane Database Syst Rev* 2015;CD002896.
9. Cukiert A. Vagus nerve stimulation for epilepsy: an evidence-based approach. *Prog Neurol Surg* 2015;29:39–52.
10. Grimm S, Bajbouj M. Efficacy of vagus nerve stimulation in the treatment of depression. *Expert Rev Neurother* 2010;10:87–92.
11. Rong P, Liu J, Wang L et al. Effect of transcutaneous auricular vagus nerve stimulation on major depressive disorder: a nonrandomized controlled pilot study. *J Affect Disord* 2016;195:172–179.
12. Ay I, Lu J, Ay H, Gregory Sorensen A. Vagus nerve stimulation reduces infarct size in rat focal cerebral ischemia. *Neurosci Lett* 2009;459:147–151.
13. Ay I, Nasser R, Simon B, Ay H. Transcutaneous cervical vagus nerve stimulation ameliorates acute ischemic injury in rats. *Brain Stimul* 2016;9:166–173.
14. Dawson J, Pierce D, Dixit A et al. Safety, feasibility, and efficacy of vagus nerve stimulation paired with upper-limb rehabilitation after ischemic stroke. *Stroke* 2016;47:143–150.
15. De Ridder D, Vanneste S, Engineer ND, Kilgard MP. Safety and efficacy of vagus nerve stimulation paired with tones for the treatment of tinnitus: a case series. *Neuromodulation* 2014;17:170–179.
16. Lehtimaki J, Hyvarinen P, Ylikoski M et al. Transcutaneous vagus nerve stimulation in tinnitus: a pilot study. *Acta Otolaryngol* 2013;133:378–382.
17. Yuan H, Silberstein SD. Vagus nerve stimulation and headache. *Headache* 2017;57:29–33.
18. Gaul C, Diener HC, Silver N et al. Non-invasive vagus nerve stimulation for PREVention and Acute treatment of chronic cluster headache (PREVA): a randomised controlled study. *Cephalalgia* 2016;36:534–546.
19. Neren D, Johnson MD, Legon W, Bachour SP, Ling G, Divani AA. Vagus nerve stimulation and other neuromodulation methods for treatment of traumatic brain injury. *Neurocrit Care* 2016;24:308–319.
20. Pruitt DT, Schmid AN, Kim LJ et al. Vagus nerve stimulation delivered with motor training enhances recovery of function after traumatic brain injury. *J Neurotrauma* 2016;33:871–879.
21. Smith DC, Modglin AA, Roosevelt RW et al. Electrical stimulation of the vagus nerve enhances cognitive and motor recovery following moderate fluid percussion injury in the rat. *J Neurotrauma* 2005;22:1485–1502.
22. Pena DF, Childs JE, Willett S, Vital A, McIntyre CK, Kroener S. Vagus nerve stimulation enhances extinction of conditioned fear and modulates plasticity in the pathway from the ventromedial prefrontal cortex to the amygdala. *Front Behav Neurosci* 2014;8:327.
23. George MS, Ward HE Jr., Ninan PT et al. A pilot study of vagus nerve stimulation (VNS) for treatment-resistant anxiety disorders. *Brain Stimul* 2008;1:112–121.
24. Sjögren M, Hellström P, Jonsson M, Runnerstam M, Silander HC-S, Ben-Menachem E. Cognition-enhancing effect of vagus nerve stimulation in patients with Alzheimer's disease: a pilot study. *J Clin Psychiatry* 2002;63:972–980.
25. Merrill CA, Jonsson MA, Minthon L et al. Vagus nerve stimulation in patients with Alzheimer's disease: additional follow-up results of a pilot study through 1 year. *J Clin Psychiatry* 2006;67:1171–1178.
26. Tronnier VM. Vagus nerve stimulation: surgical technique and complications. *Prog Neurol Surg* 2015;29:29–38.
27. Patil A, Chand A, Andrews R. Single incision for implanting a vagal nerve stimulator system (VNSS): technical note. *Surg Neurol* 2001;55:103–105.
28. Albert U, Maina G, Aguglia A et al. Vagus nerve stimulation for treatment-resistant mood disorders: a long-term naturalistic study. *BMC Psychiatry* 2015;15:64.
29. Aihua L, Lu S, Liping L, Xiuru W, Hua L, Yuping W. A controlled trial of transcutaneous vagus nerve stimulation for the treatment of pharmacoresistant epilepsy. *Epilepsy Behav* 2014;39:105–110.
30. Kraus T, Kiess O, Hösl K, Terekhin P, Kornhuber J, Forster C. CNS BOLD fMRI effects of sham-controlled transcutaneous electrical nerve stimulation in the left outer auditory canal – a pilot study. *Brain Stimul* 2013;6:798–804.
31. Silberstein SD, Calhoun AH, Lipton RB et al. Chronic migraine headache prevention with noninvasive vagus nerve stimulation: The EVENT study. *Neurology* 2016;87:529–538.
32. Silberstein SD, Mechtler LL, Kudrow DB et al. Non-invasive vagus nerve stimulation for the ACute treatment of cluster headache: findings from the randomized, double-blind, sham-controlled ACT1 study. *Headache* 2016;56:1317–1332.

33. Aalbers MW, Rijkers K, Klinkenberg S, Majoie M, Cornips EM. Vagus nerve stimulation lead removal or replacement: surgical technique, institutional experience, and literature overview. *Acta Neurochir (Wien)* 2015;157:1917–1924.
34. Helmers SL, Begnaud J, Cowley A et al. Application of a computational model of vagus nerve stimulation. *Acta Neurol Scand* 2012;126:336–343.
35. Goodall EV, Kosterman LM, Holsheimer J, Struijk JJ. Modeling study of activation and propagation delays during stimulation of peripheral nerve fibers with a tripolar cuff electrode. *IEEE Trans Rehabil Eng* 1995;3:272–282.
36. Arle JE, Carlson KW, Mei L. Investigation of mechanisms of vagus nerve stimulation for seizure using finite element modeling. *Epilepsy Res* 2016;126:109–118.
37. Arle JE, Carlson KW, Mei L, Shils JL. Modeling effects of scar on patterns of dorsal column stimulation. *Neuromodulation* 2014;17:320–333; discussion: 333].
38. Ashburner J, Friston KJ. Unified segmentation. *NeuroImage* 2005;26:839–851.
39. Huang Y, Dmochowski JP, Su Y, Datta A, Rorden C, Parra LC. Automated MRI segmentation for individualized modeling of current flow in the human head. *J Neural Eng* 2013;10:066004.
40. Wagner TA, Zahn M, Grodzinsky AJ, Pascual-Leone A. Three-dimensional head model simulation of transcranial magnetic stimulation. *IEEE Trans Biomed Eng* 2004; 51:1586–1598.
41. Deng ZD, Lisanby SH, Peterchev AV. Electric field depth-focality tradeoff in transcranial magnetic stimulation: simulation comparison of 50 coil designs. *Brain Stimul* 2013;6:1–13.
42. Bikson M, Truong DQ, Mourdoukoutas AP et al. Modeling sequence and quasi-uniform assumption in computational neurostimulation. *Prog Brain Res* 2015;222:1–23.
43. Bikson M, Dmochowski J, Rahman A. The "quasi-uniform" assumption in animal and computational models of non-invasive electrical stimulation. *Brain Stimul* 2013;6: 704–705.
44. Rubinstein JT. Axon termination conditions for electrical stimulation. *IEEE Trans Biomed Eng* 1993;40:654–663.
45. Arlotti M, Rahman A, Minhas P, Bikson M. Axon terminal polarization induced by weak uniform DC electric fields: a modeling study. *Conf Proc IEEE Eng Med Biol Soc* 2012;2012:4575–4578.
46. McIntyre CC, Grill WM. Excitation of central nervous system neurons by nonuniform electric fields. *Biophys J* 1999;76:878–888.
47. Merrill DR, Bikson M, Jefferys JG. Electrical stimulation of excitable tissue: design of efficacious and safe protocols. *J Neurosci Methods* 2005;141:171–198.
48. Warman EN, Grill WM, Durand D. Modeling the effects of electric fields on nerve fibers: determination of excitation thresholds. *IEEE Trans Biomed Eng* 1992;39:1244–1254.
49. Tranchina D, Nicholson C. A model for the polarization of neurons by extrinsically applied electric fields. *Biophys J* 1986;50:1139–1156.
50. Ranck JB. Jr. Which elements are excited in electrical stimulation of mammalian central nervous system: a review. *Brain Res* 1975;98:417–440.
51. Hines ML, Carnevale NT. The NEURON simulation environment. *Neural Comput* 1997;9:1179–1209.
52. Gasser HS, Grundfest H. Axon diameters in relation to the spike dimensions and the conduction velocity in mammalian A fibers. *Am J Physiol* 1939;127:393–414.
53. Hursh JB. Conduction velocity and diameter of nerve fibers. *Am J Physiol* 1939;127: 131–139.
54. Migliore M. Modeling the attenuation and failure of action potentials in the dendrites of hippocampal neurons. *Biophys J* 1996;71:2394–2403.
55. Bahl A, Stemmler MB, Herz AVM, Roth A. Automated optimization of a reduced layer 5 pyramidal cell model based on experimental data. *J Neurosci Methods* 2012; 210:22–34.
56. Sahin M, Tie Y. Non-rectangular waveforms for neural stimulation with practical electrodes. *J Neural Eng* 2007;4:227–233.
57. Rattay F, Paredes LP, Leao RN. Strength-duration relationship for intra- versus extracellular stimulation with microelectrodes. *Neuroscience* 2012;214:1–13.
58. Abejon D, Rueda P, del Saz J, Arango S, Monzon E, Gilsanz F. Is the introduction of another variable to the strength-duration curve necessary in neurostimulation? *Neuromodulation* 2015;18:182–190; discussion: 190.
59. Rattay F, Wenger C. Which elements of the mammalian central nervous system are excited by low current stimulation with microelectrodes? *Neuroscience* 2010;170: 399–407.
60. Mollet L, Raedt R, Delbeke J et al. Electrophysiological responses from vagus nerve stimulation in rats. *Int J Neural Syst* 2013;23:1350027.
61. Werginz P, Fried SI, Rattay F. Influence of the sodium channel band on retinal ganglion cell excitation during electric stimulation–a modeling study. *Neuroscience* 2014;266:162–177.
62. Rattay F. Analysis of the electrical excitation of CNS neurons. *IEEE Trans Biomed Eng* 1998;45:766–772.
63. Pelot NA, Behrend C, Grill W. Modeling the response of small myelinated axons in a compound nerve to kilohertz frequency signals. *J Neural Eng* 2017;14:046022.
64. Samoudi AM, Kampusch S, Tanghe E et al. Numerical modeling of percutaneous auricular vagus nerve stimulation: a realistic 3D model to evaluate sensitivity of neural activation to electrode position. *Med Biol Eng Comput* 2017;55:1763–1772.
65. Reilly JP. *Applied bioelectricity: from electrical stimulation to electropathology*. New York: Springer Science & Business Media, 2012.
66. Lerman I, Hauger R, Sorkin L et al. Noninvasive transcutaneous vagus nerve stimulation decreases whole blood culture-derived cytokines and chemokines: a randomized, blinded, healthy control pilot trial. *Neuromodulation* 2016;19:283–290.
67. Bikson M, Datta A. Guidelines for precise and accurate computational models of tDCS. *Brain Stimul* 2012;5:430–431.
68. Yoshida K, Horch K. Selective stimulation of peripheral nerve fibers using dual intrafascicular electrodes. *IEEE Trans Biomed Eng* 1993;40:492–494.
69. Rattay F, Aberham M. Modeling axon membranes for functional electrical stimulation. *IEEE Trans Biomed Eng* 1993;40:1201–1209.
70. Engel ER, Blake J, Liebler E. Non-invasive vagus nerve stimulator (gammaCore®) was not associated with meaningful cardiovascular adverse effects (P1.292). *Neurology* 2015;84:P1.292. /04/06/2015
71. Krahl SE, Senanayake SS, Handforth A. Destruction of peripheral C-fibers does not alter subsequent vagus nerve stimulation-induced seizure suppression in rats. *Epilepsia* 2001;42:586–589.
72. Capogrosso M, Wenger N, Raspopovic S et al. A computational model for epidural electrical stimulation of spinal sensorimotor circuits. *J Neurosci* 2013;33:19326–19340.
73. Parazzini M, Fiocchi S, Liorni I et al. Modeling the current density generated by transcutaneous spinal direct current stimulation (tsDCS). *Clin Neurophysiol* 2014;125: 2260–2270.
74. Howell B, McIntyre CC. Analyzing the tradeoff between electrical complexity and accuracy in patient-specific computational models of deep brain stimulation. *J Neural Eng* 2016;13:036023.
75. Stacey WC, Durand DM. Stochastic resonance improves signal detection in hippocampal CA1 neurons. *J Neurophysiol* 2000;83:1394–1402.
76. Rahman A, Reato D, Arlotti M et al. Cellular effects of acute direct current stimulation: somatic and synaptic terminal effects. *J Physiol* 2013;591:2563–2578.
77. Reato D, Rahman A, Bikson M, Parra LC. Low-intensity electrical stimulation affects network dynamics by modulating population rate and spike timing. *J Neurosci* 2010;30:15067–15079.
78. McIntyre CC, Grill WM. Selective microstimulation of central nervous system neurons. *Ann Biomed Eng* 2000;28:219–233.
79. Reilly JP, Diamant AM. *Electrostimulation: theory, applications, and computational model*. Boston, MA: Artech House, 2011.
80. Laakso I, Matsumoto H, Hirata A, Terao Y, Hanajima R, Ugawa Y. Multi-scale simulations predict responses to non-invasive nerve root stimulation. *J Neural Eng* 2014; 11:056013.
81. McIntyre CC, Grill WM, Sherman DL, Thakor NV. Cellular effects of deep brain stimulation: model-based analysis of activation and inhibition. *J Neurophysiol* 2004;91: 1457–1469.
82. Iacono MI, Makris N, Mainardi L, Angelone LM, Bonmassar G. MRI-based multiscale model for electromagnetic analysis in the human head with implanted DBS. *Comput Math Methods Med* 2013;2013:e694171.
83. Butson CR, Cooper SE, Henderson JM, McIntyre CC. Patient-specific analysis of the volume of tissue activated during deep brain stimulation. *Neuroimage* 2007;34:661–670.
84. Parrini S, Delbeke J, Romero E, Legat V, Veraart C. Hybrid finite elements and spectral method for computation of the electric potential generated by a nerve cuff electrode. *Med Biol Eng Comput* 1999;37:733–736.
85. Krasteva VT, Papazov SP, Daskalov IK. Peripheral nerve magnetic stimulation: influence of tissue non-homogeneity. *Biomed Eng Online* 2003;2:19.
86. McIntyre CC, Richardson AG, Grill WM. Modeling the excitability of mammalian nerve fibers: influence of afterpotentials on the recovery cycle. *J Neurophysiol* 2002; 87:995–1006.
87. Zhu K, Li L, Wei X, Sui X. A 3D computational model of transcutaneous electrical nerve stimulation for estimating abeta tactile nerve fiber excitability. *Front Neurosci* 2017;11:250.
88. Dmochowski JP, Datta A, Bikson M, Su Y, Parra LC. Optimized multi-electrode stimulation increases focality and intensity at target. *J Neural Eng* 2011;8:046011.
89. Hammond EJ, Uthman BM, Reid SA, Wilder BJ. Electrophysiologic studies of cervical vagus nerve stimulation in humans: II. Evoked potentials. *Epilepsia* 1992;33:1021–1028.
90. Nonis R, D'Ostilio K, Schoenen J, Magis D. Evidence of activation of vagal afferents by non-invasive vagus nerve stimulation: an electrophysiological study in healthy volunteers. *Cephalalgia* 2017;333102417717470.
91. Jog MV, Smith RX, Jann K et al. In-vivo imaging of magnetic fields induced by transcranial direct current stimulation (tDCS) in human brain using MRI. *Sci Rep* 2016;6: 34385.
92. Huang Y, Liu AA, Lafon B et al. Measurements and models of electric fields in the in vivo human brain during transcranial electric stimulation. *eLife* 2017;6: e18834.

